ORIGINAL RESEARCH

# Herb–Nanoparticle Hybrid System for Improved Oral Delivery Efficiency to Alleviate Breast Cancer Lung Metastasis

Jiangpei Shi[1],*, Rongguang Zhang[1],*, Yu Wang[1], Yingwei Sun[1], Xiaoyan Gu[1], Yu An[1], Xinyu Chai[1], Xiaoyu Wang[2], Zhi Wang[1], Yaqi Lyu[1], Teng Guo[1], Nianping Feng 🔵[1], Ying Liu[1]

[1]School of Pharmacy, Shanghai University of Traditional Chinese Medicine, Shanghai, 201203, People's Republic of China; [2]Experiment Center for Science and Technology, Shanghai University of Traditional Chinese Medicine, Shanghai, 201203, People's Republic of China

*These authors contributed equally to this work

Correspondence: Nianping Feng; Ying Liu, Email npfeng@shutcm.edu.cn; debbyly@shutcm.edu.cn

**Background:** Metastasis is a complex process involving multiple factors and stages, in which tumor cells and the tumor micro-environment (TME) play significant roles. A combination of orally bioavailable therapeutic agents that target both tumor cells and TME is conducive to prevent or impede the progression of metastasis, especially when undetectable. However, sequentially over-coming intestinal barriers, ensuring biodistribution in tumors and metastatic tissues, and enhancing therapeutic effects required for efficient therapy remain challenging.

**Methods:** Inspired by the unique chemical features of natural herbs, we propose an oral herb–nanoparticle hybrid system (HNS) formed through the self-binding of *Platycodon grandiflorum–Curcuma zedoaria* (HG), a herb pair/group used in clinical practice to treat breast cancer metastasis, to lipid–polymer nanoparticles (LPNs) loaded with silibinin. The molecular structure responsible for HG association with LPNs was assessed using surface-enhanced Raman spectroscopy for HNS surface chemistry characterization. Moreover, the molecular class of HG was identified using UPLC–Orbitrap–MS/MS to further confirm the surface binding. Mucus diffusion and in vivo biodistribution were evaluated using in vitro multiple-particle tracking and environment-responsive fluorescence probe in 4T1 tumor-bearing mice, respectively. The alleviation of breast cancer metastasis was assessed in 4T1 tumor-bearing mice, and the underlying mechanism was investigated.

**Results:** The HNS reduced particle–mucus interactions by altering hydrophilicity and surface characteristics compared to LPNs. The epithelium transportation of HNS and absorption through Peyer's patch in mice were improved, promoting their biodistribution in the lung and tumor tissues. Furthermore, the HNS alleviated lung metastasis by inducing cell apoptosis and regulating the expression of MMP-9 and TGF-β1, which altered the TME in 4T1 tumor-bearing mice.

**Conclusion:** HNS provides an appealing system with multi-component binding of herbal medicine to facilitate both oral nanoparticle delivery efficiency and the alleviation of lung metastasis. This strategy may potentially help improve treatment for patients with breast cancer.

**Keywords:** herb–nanoparticle hybrid system, intestinal biological barrier, tumor microenvironment, breast cancer lung metastasis

## Introduction

Breast cancer metastasis is a complex biological process involving multiple pathways and stages.[1] Tumor cells closely interact with the tumor microenvironment (TME), which is responsible for tumor growth and the transition from the undetectable phase of metastasis to overt metastasis.[2] Regulation of TME as a strategy to inhibit breast cancer metastasis has attracted attention. Some advanced nanocarriers against cancer metastasis that can regulate TME have been developed, and various administration routes have been evaluated to improve their delivery efficiency.[3–5] Among the possible routes, oral administration is convenient and flexible. It may improve the patient's quality of life that is affected

by the disease's chronic and aggressive nature, which is beneficial for the treatment of breast cancer.[6,7] Therapeutic agents loaded onto oral nanocarriers offer possibilities for preventing or inhibiting the progression of breast cancer metastasis. However, the limited diffusion of nanoparticles into the systemic circulation owing to physiological barriers and their poor distribution at the site of action limit the benefits of oral nanocarriers. Therefore, sequentially overcoming the intestinal barriers, improving biodistribution in tumors and metastatic tissues, and enhancing therapeutic effects remain core challenges.

In recent years, lipid–polymer nanoparticles (LPNs) have emerged as a promising oral drug delivery system, given their desirable biocompatibility and drug loading and release capacity. Several functional LPNs have been developed through modification with hydrophilic polymers and surfactants to achieve mucus diffusion and overcome intestinal barriers.[8,9] However, these materials are pharmacologically inert, with negligible or no therapeutic effects against tumor metastasis. In addition to entering the systemic circulation, the distribution of drugs and nanocarriers at tumor and metastatic sites is indispensable for improving therapeutic effects. Therefore, alternative strategies for fabricating advanced LPNs to improve oral delivery efficiency and enhance their therapeutic effects are urgently needed.

Natural herbs generally contain multiple compounds, including hydrophilic, hydrophobic, and amphiphilic compounds, with various physiochemical properties. Bioactive components from a natural origin, such as polyphenols, saponins, and polysaccharides, can aid in the formation of nanoparticles via self-assembly or molecular interactions.[10] Structurally, LPNs have a hydrophobic core and hydrophilic shell. LPN may possess positive or negative charge based on the surface components. Therefore, inspired by the unique characteristics of herbal medicines, we hypothesized that multiple components in the herb would bind with one LPN, thereby forming a herb–nanoparticle hybrid system (HNS) and altering their biological fate in vivo. Compared with nanoparticle binding with the previous single component, the binding generated from a mixture of herbs is expected to exert superior therapeutic action in a systemic and integrative manner.

Herbs *Platycodon grandiflorum* and *Curcuma zedoaria* (referred to as HG) have been used as a highly valuable medicinal herb pair/group in the treatment of breast cancer metastasis in clinical practice, as the pair regulates the TGF-β/SMAD signaling pathway and suppresses the secretion of transforming growth factor β1 (TGF-β1) and matrix metalloproteinases (MMPs).[11] *Platycodon grandiflorum* can inhibit breast cancer metastasis by inhibiting cell proliferation, migration, and invasion,[12,13] via a mechanism involving the regulation of interleukin (IL)-6, IL-8, MMP-1, and the chemokine CXCL1, and suppressing the expression of TGF-β1 and a related protein, SMAD7.[14,15] *Curcuma zedoaria* belongs to the Zingiberaceae family. Active components of *Curcuma zedoaria*, such as germacrone and furanodiene, can inhibit the proliferation, invasion, and metastasis of breast cancer cells.[16] In addition to its pharmacological effects, HG can aid in delivering other prescribed therapeutic agents to the lungs, thus potentiating their therapeutic effects.[14] HG reduces the toxicity of chemotherapeutic agents, active components of traditional Chinese medicine, and compound Chinese medicines and acts synergistically against tumor-related diseases; for example, HG promotes the pulmonary distribution of cisplatin and reduces the distribution of doxorubicin in heart tissues.[17] Platycodin D, a component of *Platycodon grandiflorum*, plays a role in this guided delivery.[18] In addition, a recent study has reported a potent pulmonary targeting ability for nanoparticles composed of *Platycodon* polysaccharides compared with those composed of other polysaccharides.[19] However, to our knowledge, whether HG can bind to LPNs to form a hybrid system and alter the biological fate, particularly in absorption, transportation and distribution of LPNs, has not been investigated. Furthermore, given the therapeutic components contained in this system, whether the hybrid system can enhance therapeutic effects because of the combination of HG with TME-regulating therapeutic agents loaded in LPNs remains unknown.

Silibinin, an active component of *Silybum marianum* (L). Gaertn., can regulate TME by modulating epithelial–mesenchymal transition (EMT), reducing tumor microvascular density, inhibiting angiogenesis, reducing extracellular matrix (ECM) decomposition, and inhibiting collagen formation in tumor tissues.[20,21] Silibinin acts by inhibiting the activity of TGF-β and MMPs.[22] The potency of silibinin-loaded (or co-loaded with active ingredients) orally administered LPNs against breast cancer metastasis has been investigated. Detachable hydrophilic polymers or sophorolipids have been used to achieve bioresponsive mucus diffusion and overcome intestinal barriers.[8,9] Based on these previous

studies, improving the biodistribution of silibinin-loaded LPNs in tumor and metastatic tissues and enhancing the therapeutic effects are important issues that need to be addressed.

Dual action of inhibiting the proliferation of tumor cells and regulating TME are effective strategies in mitigating breast cancer metastasis; therefore, in this study, we developed a novel oral delivery system, the natural HNS, formed from silibinin-loaded LPNs and herb pair (Scheme 1), in which silibinin is expected to regulate TME and HG is expected to inhibit tumor cells. Owing to the unique characteristics and chemical components of HG, the multiple components in the HG may bind with LPNs, and change the surface hydrophilicity and surface components, thus influencing the fate of transfer in the gastrointestinal tract and distribution at the site of action. Therefore, we focused on revealing the surface chemistry and investigating the promotion of oral nanoparticle delivery efficiency in terms of mucus diffusion and biodistribution. Furthermore, their therapeutic potential for alleviating breast cancer metastasis was assessed in 4T1 tumor-bearing mice.

# Materials and Methods
## Reagents
Silibinin (purity > 98.0%) was obtained from Dalian Meilun Biotech (Dalian, Liaoning, China). Lipoid S100 was obtained from Lipoid GmbH (Ludwigshafen, Germany). DSPE-PEG2000 [(1,2-Distearoyl-sn-glycero-3-phosphoethanol-amine-N-methoxy (polyethylene glycol)-2000)] was obtained from AVT Technology (Shanghai, China). PLGA (50/50, Mw 50 kDa) was provided by Dalian Meilun Biotechnology Co., LTD (Dalian, China). P2 was kindly provided by Professor Wu Wei from the School of Pharmacy, Fudan University, Key Laboratory of Smart Drug Delivery of MOE and PLA (Shanghai, China). DiI (1,1'-dioctadecyl-3,3,3',3'tetramethylindocarbocyanine perchlorate) was obtained from Thermo Fisher Scientific (Rockford, IL, USA). CdSe/ZnS hydrophobic quantum dots were obtained from Mukenano (Nanjing, China). AgNPs dispersion was from XFNANO (Nanjing, China). Antibodies against PE-CD3ε, fluorescein isothiocyanate-CD8a, PE/Cy7-CD45, AHG-CD4, AHG-Gr-1, AHG I-A/I-E, and Alexa Fluor® 488-CD11b were acquired from BioLegend.
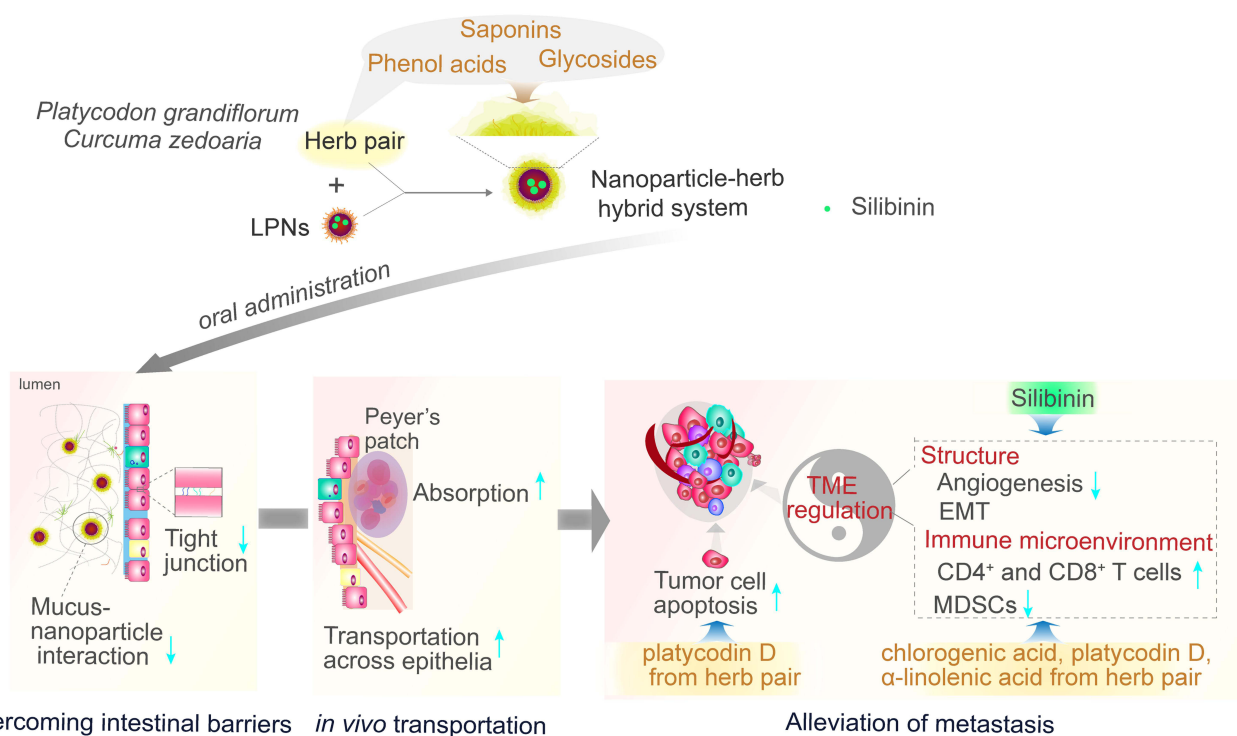


**Scheme 1** Schematic of the dual action of herb association by promoting the oral delivery efficiency of nanoparticles and enhancing therapeutic effect against breast cancer metastasis.

Platycodonis Radix (Latin scientific name: *Platycodon grandiflorum* [Jacq.] A. DC) and *Curcuma rhizome* (Latin scientific name: *Curcuma zedoaria* [Berg.] Rosc) were administered in dried radix and rhizome forms, respectively. Platycodonis Radix (Lot: 191028; Anhui) and Curcuma rhizome (Lot: 190910; Zhejiang) were both purchased from Kangqiao Co. (Shanghai, China) in the form of ready-to-use decoction pieces. Both herbs met the criteria and standards of Chinese Pharmacopoeia 2020 Edition.

## Cell Culture and Animals

HT29-MTX-E12 cells were purchased from the European Collection of Authenticated Cell Cultures (Salisbury, UK). Caco-2 and 4T1 cells were obtained from the Shanghai Institutes for Biological Sciences (Shanghai, China).

Animal studies were performed according to the guidelines of the Institutional Animal Care and Use Committee of the Shanghai University of Traditional Chinese Medicine (Approval Number (PZSHUTCM201113007, PZSHUTCM210115013)). All animals were provided by the Shanghai University of Traditional Chinese Medicine and housed and bred under standard conditions. Mice (BALB/c, female, aged 6–8 weeks) were used for nanoparticle uptake by the villi, in vivo Peyer's patch absorption, and anti-metastasis efficacy studies. Female rats (200 ± 20 g) were used for pharmacokinetic studies.

## Fabrication of the Herb–Nanoparticle Hybrid System

First, LPN nanoparticles were prepared according to a modified nanoprecipitation method as previously reported.[9] Lipoid S100 and DSPE-PEG2000 (2:3, *w/w*) were dissolved in absolute alcohol, introduced to deionized water (65 °C), and gently stirred for 0.5 h. PLGA and silibinin were dissolved in acetonitrile as an oil phase (5 mg/mL). The oil phase was added to the aqueous dispersion (1:2, *v/v*) while gently stirring for 2 h at 25 °C. Then, acetonitrile was removed using the rotary evaporator. The mixture was passed through a 0.8-μm filter. *Platycodon grandiflorum* and *Curcuma zedoaria* pieces (1:2, *w/w*) were soaked in water for 0.5 h. Then, they were decocted twice with a six-fold volume of water for 1 h. The decoctions were collected and filtered through a 0.8-μm filter membrane to obtain HG. The HNS was obtained by mixing the LPN dispersion with HG (1:1, *v/v*) via gentle agitation at 25 °C for 2 h.

The zeta potential was measured in a Zetasizer Nano ZS90 (Malvern Instruments, Malvern, UK). To determine the particle size, coumarin-6-loaded LPNs were diluted with deionized water (1:10,000). The particle concentrations and intensities were then determined using Nanosight NS300 (Malvern Instruments, Malvern, UK). Particle morphology was observed via TEM (Tecnai G2 Spirit; FEI Ltd., Hillsboro, USA). The nanoparticle dispersion was diluted with deionized water, dropped on the copper grids, and negatively stained with 2% (w/v) phosphotungstic acid. Encapsulation and drug loading were determined according to the previously reported ultrafiltration method. The details are shown in the Supporting Information.

## Surface Chemistry Characterization

An emerging spectroscopic characterization technique, SERS, was used to assess the surface chemistry of the HNS. Before SERS determination, the test samples were prepared as follows: individual herb decoctions of *Platycodon grandiflorum* and *Curcuma zedoaria* were prepared using the same method as that for herb decoction in the section of Fabrication of the Herb–nanoparticle Hybrid System. Then, each decoction was freeze-dried using freeze dryer (Labconco, MO, USA). Briefly, after pre-freezing at −20 °C overnight, the sample was transferred to the freeze dryer and lyophilized with a vacuum pressure of 3.0 Pa at −40 °C. The lyophilized powder was dispersed in deionized water (80 mg/mL) and treated in an ultrasonic bath (40 kHz, 150 W) for 30 min. The sample was then centrifuged at 2486×g for 3 min, and the supernatant was collected for determination. The HNS dispersion was transferred to a pretreated dialysis bag (molecular weight cutoff 14 kDa), which was covered with PEG20000 to remove the free components in the HG. The sample was then redispersed in deionized water. SERS spectra of individual herb decoctions, HG decoctions, LPN dispersion, and HNS dispersion were collected under the following conditions: 20 μL of AgNPs dispersion was dropped on the silicon wafer (20 × 20 mm, BZS2020, Beijing Zhongjingkeyi Technology Co., Ltd, Beijing, China), followed by dropping 20 μL of sample dispersion and mixing to form a spot. Then, the spot was air-dried at 25 °C before detection below the laser. The Raman spectrometer (Titan Electro-Optics Co., Ltd, Beijing, China) was used to detect the

spectra. The Raman microscope system was coupled with a DM2700M microscope (Leica Microsystems, Wetzlar, Germany), equipped with a 50× optical objective. The spectra were collected with a CCD detector array (2000 × 256). The detection grating was set at 600. The laser source was 785 nm with a laser power of 10–25 mv. The spectral bands were recorded over a range of 540–1722 $cm^{-1}$, with a spectral resolution of 5 $cm^{-1}$; the signal acquisition time was 20s, and each sample was parallel measured three times.

The spectra were processed using the software Labspec5 (Horiba). According to a previous report,[23] the SERS spectra were smoothed and denoised (degree, size, and height were set as 4, 5, and 50, respectively), and baseline corrected (type, degree, and attach were set as polynom, 6, and no, respectively; auto pattern). Each spectrum was normalized by scaling the intensity of SERS spectrum between 0 and 1 to avoid differences in the intensities during acquisition.[23] The SERS spectrum was plotted using Origin Pro2023 (Origin Lab Corp., Northampton, MA, USA).

## UPLC-LTQ-Orbitrap MS Analysis

UPLC-LTQ-Orbitrap MS was performed to verify SERS results. Freeze-dried HG powder was extracted from methanol, followed by centrifugation at 1500×g for 10 min at 4 °C. The supernatant was then withdrawn and filtered through a 0.22 μm filter prior to analysis. The Thermo Scientific UltiMate 3000 HPLC system and Orbitrap Elite system (Thermo Fisher Scientific, Waltham, MA, USA) were coupled for chromatographic separation and MS detection. A Waters ACQUITY UPLC HSS T3 (100 mm × 2.1 mm, 1.8 μm) column was used. The chromatographic conditions were set as follows: mobile phase composed of formic acid water (0.1%. v/v) (line A) and acetonitrile (line B). Elution gradient program: 0–0.5 min, 2% B; 0.5–2 min, 2–5% B; 2–3 min, 5–15% B; 3–13 min, 15–50% B; 13–25 min, 50–95% B; 25–30 min, 95% B; 30–30.5 min, 95–5% B; 30.5–35 min, 5% B. The flow rate was 0.3 mL/min, injection volume was 4 μL, and column temperature was 40 °C. The mass spectrometer was equipped with an electrospray ionization source. Operation parameters used in positive and negative ionization modes were as follows: source temperature, 300 °C; sheath gas, 35 (arbitrary units); auxiliary gas, 15 (arbitrary units); sweep gas, 0 (arbitrary units) (+) and 1 (arbitrary units) (−); electrospray voltage, 3.8 kV(+) and 3.2 kV(−); capillary temperature, 350 °C; S-Lens RF value, 30% (+) and 60% (−). The MS analysis was operated in the data-dependent acquisition mode. The spectra were acquired at an MS resolution of 60,000 and MS2 of 15,000 by scanning from m/z 50 to 1500 in the FT mode.

The raw data were obtained and processed using Xcalibur workstation, Compound Discoverer 3.3 software, the local Chinese medicine component high-resolution mass spectrometry database (OTCML), and mzCloud-Advanced Mass Spectral Database (workstation, software, and database are from Thermo Fisher Scientific, Waltham). Data with a calculation error exceeding 5 ppm (except Platycodin D −7.88 ppm) were removed.

## Isothermal Titration Calorimetry Assay

To investigate the molecular interactions between platycodin D and DSPE-PEG2000, the heat flow during the binding of platycodin D to DSPE-PEG2000 was determined via ITC assay using the MicroCal iTC 200 system (Malvern Panalytical, UK). The details are provided in the Supporting Information.

## Stability of HNS in Simulated Gastric Fluid and Simulated Intestinal Fluid

Prior to the evaluation of stability, SGF and SIF were prepared as previously reported.[8] Briefly, 16.4 mL of hydrochloric acid solution (from 100 mL solution containing 23.4 mL of concentrated hydrochloric acid in deionized water) was diluted in deionized water to obtain 1000 mL of SGF. SIF was prepared as follows: 500 mL of potassium dihydrogen phosphate solution was prepared by dissolving 6.8 g potassium dihydrogen phosphate in deionized water, followed by adjusting to pH 6.8 using 0.1 M sodium hydroxide and adding deionized water to the total volume of 1000 mL. The stability of HNS in SGF or SIF was evaluated by mixing HNS dispersion with SGF or SIF (1:9, *v/v*) and incubating at 37 °C. Then, the mean particle size and zeta potential were measured at 0, 2, 4, 6, and 8 h.

## In vitro Mucus Transfer

The nanoparticle motion of the HNS was studied via multiple-particle tracking (MPT) as previously described.[24] In addition, to determine whether HNS has a lower interaction between endogenous mucus components and nanoparticles,

NanoSight analysis (NTA) was performed using coumarin-6-loaded nanoparticles. The detailed descriptions of MPT and NTA are provided in the Supporting Information.

## Nanoparticle Uptake by the Villi and Absorption in Peyer's Patches in Mice

Coumarin-6- or Dil-labeled nanoparticles (HNS or LPN) were prepared with fluorescent labels replacing silibinin. Prior to the experiment, the mice were administered a liquid diet for 48 h, followed by 24 h of fasting with *ad libitum* access to water. The animals were anesthetized with urethane. An incision was made in each abdomen, and the jejunum (approximately 2 cm) was exposed. After the ligation of one end with a suture, 400 μL of the prepared reagent comprising equal volumes of coumarin-6- and Dil-labeled nanoparticles was sealed into the jejunum through ligation. The segment was gently washed with saline and excised. Sections of approximately $10 \times 10$ mm$^2$ were prepared, gently loaded into a laser confocal cell culture dish, and observed using CLSM. Scanning was conducted at 10-μm intervals along the z-axis to determine the nanoparticle diffusion and uptake by the villi.

Subsequently, the regulation of tight junctions between the epithelial cells by HNS was evaluated using the following procedure. Caco-2/HT29-MTX-E12 cells were cultured in 12-well Transwell inserts until confluent cell monolayers were formed. FITC-dextran (MW = 4 kDa; FD-4) was used as a fluorescent marker of transport across the monolayers. The FD-4 (1.0 mg/mL) and/or HG (0.25 mg/mL) in HBSS was added to the apical sides, and HBSS was added to the basolateral sides. After incubation at 37 °C for 2 h, cells were fixed with paraformaldehyde solution and then gently rinsed in cold PBS. The membranes were sectioned, embedded in optimal cutting temperature, incubated in 1 mg/mL RNAse for 25 min, stained with propidium iodide, and visualized under a TCS SP8 confocal system (Leica Microsystems GmbH, Wetzlar, Germany) equipped with tetramethyl rhodamine isothiocyanate and FITC channels (red fluorescence for propidium iodide and green for FD-4).

Nanoparticle lymphatic absorption was visualized in BALB/C mice (20–22 g) as previously described.[25] The detailed description of the Peyer's patch absorption is present in the Supporting Information.

## In vivo Translocation of Nanoparticles into the Systemic Circulation and Subsequent Biodistribution

P2-labeled nanoparticles were prepared using the same method described in the Section of Fabrication of the Herb–nanoparticle Hybrid System, except for P2, which was dissolved in dichloromethane and added to the organic phase. The HG decoction containing 100 mg/mL *Platycodon grandiflorum* and 200 mg/mL *Curcuma zedoaria* was used to yield the HNS for pharmacokinetic and biodistribution studies.

For the pharmacokinetic study, female Sprague Dawley rats (weighing $200 \pm 20$ g) were housed under standard conditions and fed a normal diet with *ad libitum* access to water. Prior to the experiments, the animals were fasted overnight but with free access to water. The pharmacokinetic studies in rats were performed in accordance with a previous method.[26] Dispersions of P2-labeled LPNs or HNS (both nanoparticles containing P2 16.7 μg/mL) were administered to rats by gavage. Blood (200 μL) was collected from the venous plexus at 0, 4, 8, 12, 16, 20, and 24 h after the gavage and added to the wells of black 96-well plates. Then, P2 fluorescence signals in the blood samples were detected using an IVIS Lumina XR system (Perkin Elmer, Waltham, USA), with excitation wavelengths set at 710 nm.

For the biodistribution study, BALB/c mice (female, 20–22 g) were used. The 4T1-induced tumor model was established by orthotopic injection of $4 \times 10^5$ cells/mouse into the second mammary fat pad pair. On day 22 post-inoculation, 0.2 mL P2-labeled LPN dispersion or HNS (both nanoparticles containing P2 16.7 μg/mL) was administered to mice (0.1 mL/10 g) by gavage. The animals were sacrificed via cervical dislocation at the time point of 1, 2, 4, 8, 12, and 24 h. The tissues and organs (liver, lungs, heart, spleen, kidneys, mesentery, and tumor) were dissected and isolated. Images were captured using the IVIS Lumina XR imaging system (Ex 710 nm). To quantify the distribution of the nanoparticles in the tumors and lung tissues, the tissues were carefully cut into approximately $1 \times 1 \times 1$ mm$^3$ pieces and placed in the wells of black 96-well plates. P2 fluorescence signals were detected using the in vivo imaging system.

## In vivo Anti-Metastasis Efficacy Studies

BALB/c mice (female, 20–22 g) were randomly assigned to four groups. The 4T1-induced tumor model was established via an orthotopic injection of $4 \times 10^5$ cells/mouse into the second mammary fat pad pair. After 2 days, the animals were treated with saline, HG, LPNs, or HNS by gavage. The treatments were performed every 2 days, a total of 12 times at a dose of 80 mg/kg.[9] After the 12th dose, the animals were euthanized via cervical dislocation. The tumors, lungs, hearts, spleens, livers, and kidneys were excised and fixed in paraformaldehyde, then embedded in paraffin, followed by an H&E assay. The immune cells in the TME of the tumor tissues were investigated using flow cytometry. Immunohistochemical (IHC) assays were performed in the tumor and lung tissues to measure the expression levels of MMP9 and TGF-1β. The myeloid-derived suppressor cells (MDSCs) in the tumor tissues were evaluated using immunofluorescence staining. The details of the flow cytometry assay, IHC assay, and immunofluorescence staining are described in the Supporting Information.

## Statistical Analysis

Data are presented as the mean ± standard deviation (SD). The unpaired two-tailed *t*-test was selected for two-group comparisons. One-way analysis of variance with Tukey's test was used for multiple comparisons using GraphPad Prism software. Statistical significance was set at $p < 0.05$.

# Results and Discussions

## Construction and Characterization of HNS

A schematic of HNS is shown in Figure 1A. First, the morphology, particle size, and zeta potential of the HNS were determined and compared with those of LPNs. As shown via transmission electron microscopy (Figure 1B), LPNs were spherical or near-spherical in shape, with a clear shell–core structure. As for the HNS, the nanoparticles maintained a spherical shape (Figure 1B). However, the distinct boundary of the nanoparticle shell around the bright white core became unclear. Moreover, an irregular "flower"-like outline appeared on the surface of the nanoparticles. The HNS showed a lower absolute zeta potential (Figure 1C) and higher mean particle size than LPNs (Figure 1C). The reduced absolute zeta potential might be due to the association of components from HG, such as phenolic acids. Transmission electron micrographs and the particle size as well as the polydispersity index (PDI) of the HNS compared with those of LPNs suggested an interaction between LPNs and HG. Therefore, we hypothesized that some components in the HG may interact with the lipid shell of LPNs and change the regular arrangement of Lipoid S100 and DSPE-PEG2000 at the particle surface. In addition, the nanoparticle loaded with silibinin showed encapsulation efficiency of 94.75% and drug loading of 6.48%.

## Surface Chemical Components of HNS

In this study, to investigate LPN–HG interaction, we first performed surface-enhanced Raman spectroscopy (SERS) to reveal the molecules in HG associated with LPNs. Then, UPLC-LTQ-Orbitrap MS was performed to identify the chemical constituents in herb pair and support the results of SERS. Furthermore, based on SERS and UPLC-MS analyses, from the thermodynamic aspect of molecular interactions, platycodin D, a chemical component of HG, was selected as a representative substance to monitor its binding with DSPE-PEG2000, which was located at the surface of LPNs using isothermal titration calorimetry (ITC).

To understand the surface chemistry of the HNS and verify the binding of the HG with LPNs, we performed an in situ SERS analysis. SERS is a reliable and nondestructive analytical spectroscopic technique. It provides fingerprint information of molecules by analyzing the molecular structure of rotational and vibrational modes from energy exchange during inelastic collision. In recent years, several studies have applied SERS to determine the structure and chemical composition of TCM components for elucidating geographic origins, compatibility of multiple prescriptions, and residues in Chinese materia medica.[27] Importantly, as a highly sensitive analytical technology, SERS is useful for detecting and discriminating the external layer from the rest of the nanoparticle, as SERS amplification generally fails beyond several tens of nm away from the nanoparticle surface. Therefore, it provides in situ information on the orientation and binding
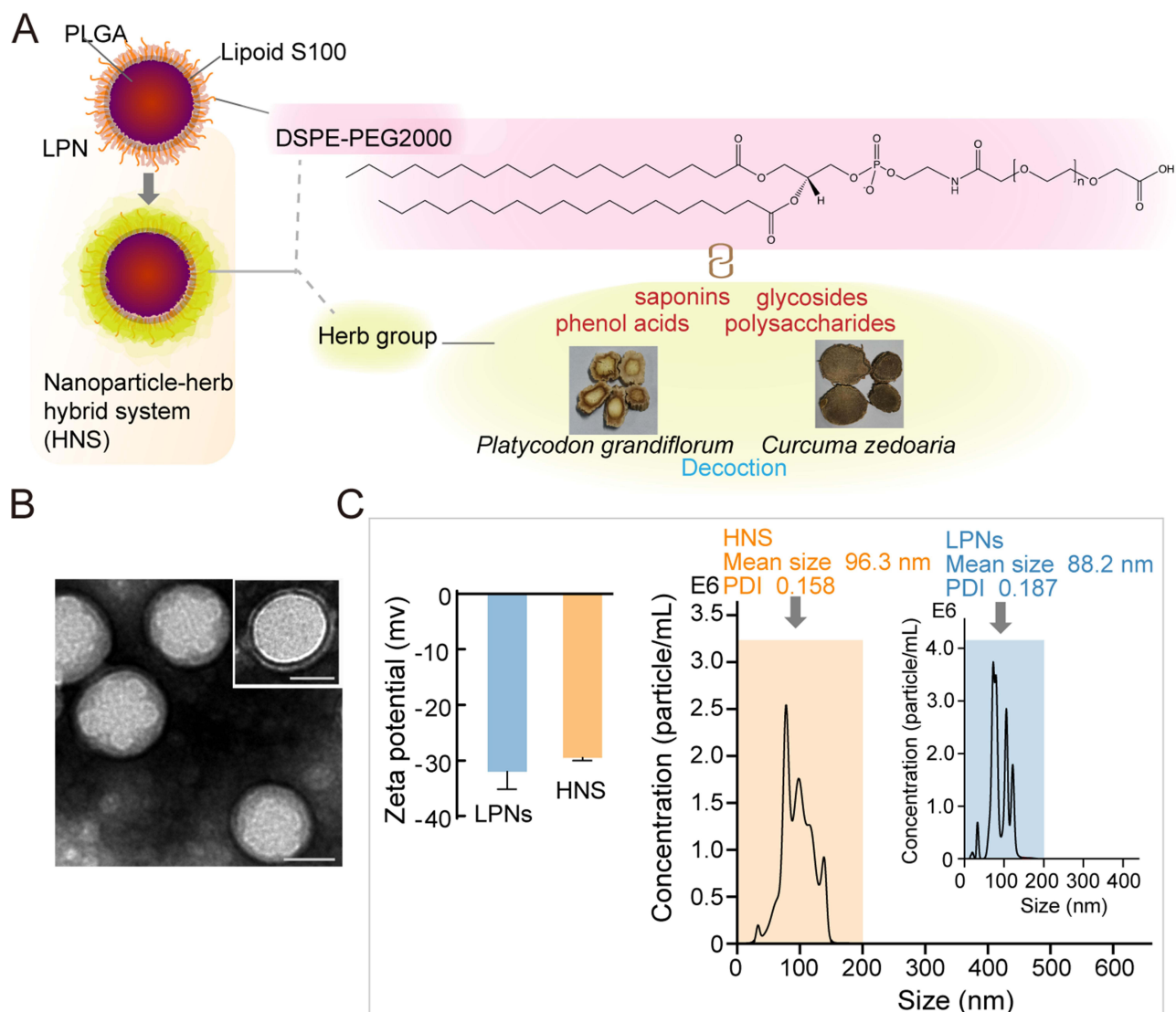
**Figure 1** Fabrication and characteristics of the herb–nanoparticle hybrid system (HNS). (**A**) Schematic of the HNS. (**B**) Transmission electron micrographs of the HNS and lipid-polymer nanoparticles (LPNs) (upper right) (scale bar, 50 nm). (**C**) Zeta potential and particle size determined via coumarin-6-labeled nanoparticle tracking analysis.

between chemical substances and the surface of nanoparticles.[28] The typical SERS bands are displayed in Figure 2. In LPNs, 891 cm$^{-1}$ and 940 cm$^{-1}$ were assigned to skeletal deformation vibration, 1077 cm$^{-1}$ to C-C vibrations, and 1100–1500 cm$^{-1}$ to CH$_2$ vibration mode.[29] The HNS showed more chemical species than HG-free LPNs. The HNS showed different band vibrations in both number and relative intensity initially, implying that the HNS and LPNs have different surface layer compositions. Compared with that in HG, the strong intensification of the bands in HNS at 825 cm$^{-1}$, 1002 cm$^{-1}$, 1188 cm$^{-1}$, and 1590 cm$^{-1}$ revealed their interactions via HG attachment on LPNs. Furthermore, the appearance of new bands at 1170 cm$^{-1}$ compared to HG, *Platycodon grandiflorum*, and *Curcuma zedoaria* suggests that an alternative association may exist, which may undergo chemical changes through some structural points. Subsequently, we determined the class of chemicals for the associated molecules and how the association occurred through a comparison of the profiles of the HNS with individual herbs and the HG. The HNS had Raman peaks at 622 cm$^{-1}$, 1030 cm$^{-1}$, and 1220 cm$^{-1}$, which were consistent with those in the *Platycodon grandiflorum* spectrum. These peaks were reported to be the typical peak of saponins,[30,31] indicating that saponins were contained in the surface layer of the HNS. Furthermore, in the HNS, carboxylate and phenol group motion was clearly identified. The presence of bands at
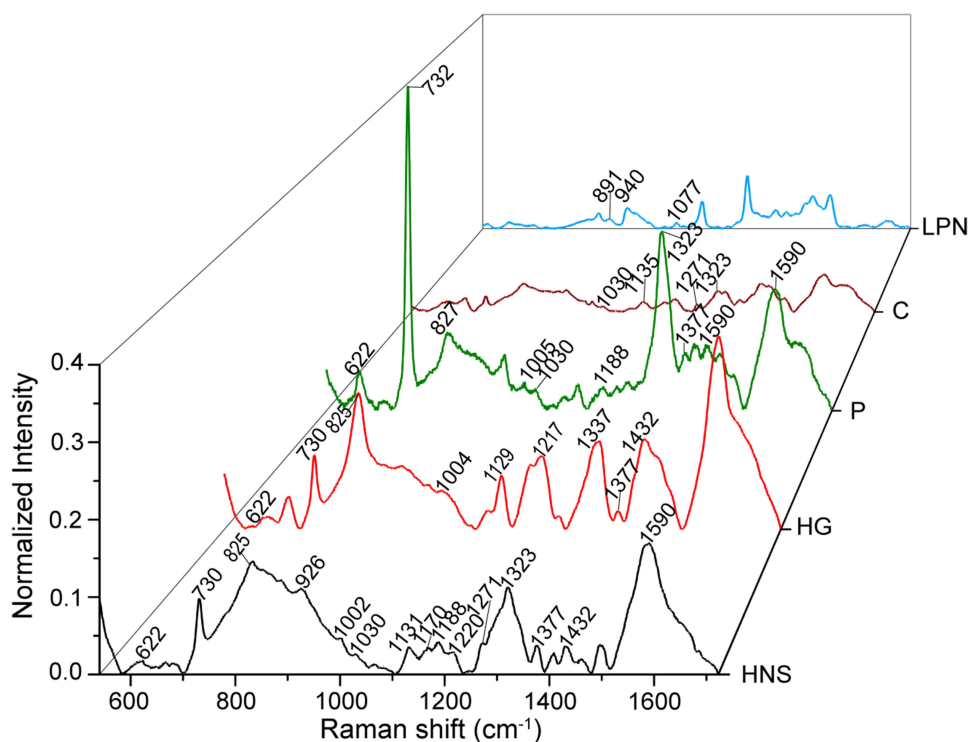
**Figure 2** Surface-enhanced Raman scattering spectra of the HNS, HG (herb pair), P (*Platycodon grandiflorum*), C (*Curcuma zedoaria*), and LPNs (laser source 785 nm, Raman spectral shifts from 540 to 1722 cm⁻¹).

1188 cm⁻¹, 1220 cm⁻¹, 1271 cm⁻¹, and 1377 cm⁻¹ indicated plane C-H bending, C-O in phenol, C-O in aromatic ethers, and ν (COO⁻), respectively. The strong band at 1377 cm⁻¹ might have resulted from the association of the carboxylic acid. Together with the band at 1590 cm⁻¹ $ν_{as}$ (COO-), this indicates that the carboxylate group takes part in the association. The vibration at around 730 cm⁻¹ was also related to polyphenols.[32] In addition, a downshift in the phenol from 1223 cm⁻¹ to 1217 cm⁻¹ and the weakened signal of 1637 cm⁻¹ [ν (C-C), ν (C-O)] was attributed to the rupture of internal H bonds between the phenol and carboxylate groups once they attached to the surface of the nanoparticle.[33] SERS spectrum of the HNS also showed vibrations at 1131 cm⁻¹ (C-O-stretching), 926 cm⁻¹ (-C-O-C- stretching), and 1550–1650 cm⁻¹ (benzene ring skeleton), which indicated the chemical groups of glycosides.[27] The peak at around 1322–1324 cm⁻¹ was possibly generated by the bending vibrations of the carbohydrate CH₂ group, which was highly related to sugars from polysaccharides.[32] Moreover, according to the chemical information, several peaks observed in the spectra for *Platycodon grandiflorum, Curcuma zedoaria*, or HG (937 cm⁻¹, 1244 cm⁻¹, 1251 cm⁻¹, 1334 cm⁻¹, and 1453 cm⁻¹) were not present in the spectrum of the HNS, indicating that these molecules were not attributed to the HNS. All the peaks identified during SERS are presented in Supplemental Table S1. Collectively, saponins, phenol acids, glycosides, and polysaccharides may take part in the HNS association.

To support the results of SERS and verify these components in the HG, we identified the chemical compositions of the HG through UPLC-MS/MS. The total ion chromatograms of the HG are shown in Figure 3. Supplemental Tables 2 and 3 present the detailed mass spectrometry data of the identified compounds. In total, 87 compounds were identified from the HG in the positive and negative ionization modes, including 30 organic acids and phenolic acids, 16 sesquiterpenoids, 8 aldehydes and ketones, 1 saponin, 1 glycoside, 2 lactones, 7 amino acids and their derivatives, 4 phenols, 3 nucleosides, and 15 other chemical types. Seven representative compounds from phenolic acids, saponins, glycosides, flavonoids, amino acids, sesquiterpenoids, and nucleosides in the HG were used to verify the identification. Their proposed fragmentation pathways are presented in Figures S1–S7. Their cleavage information is provided in the Supplemental Material. The chemical components found in the UPLC-Orbitrap MS/MS analysis covered those assigned
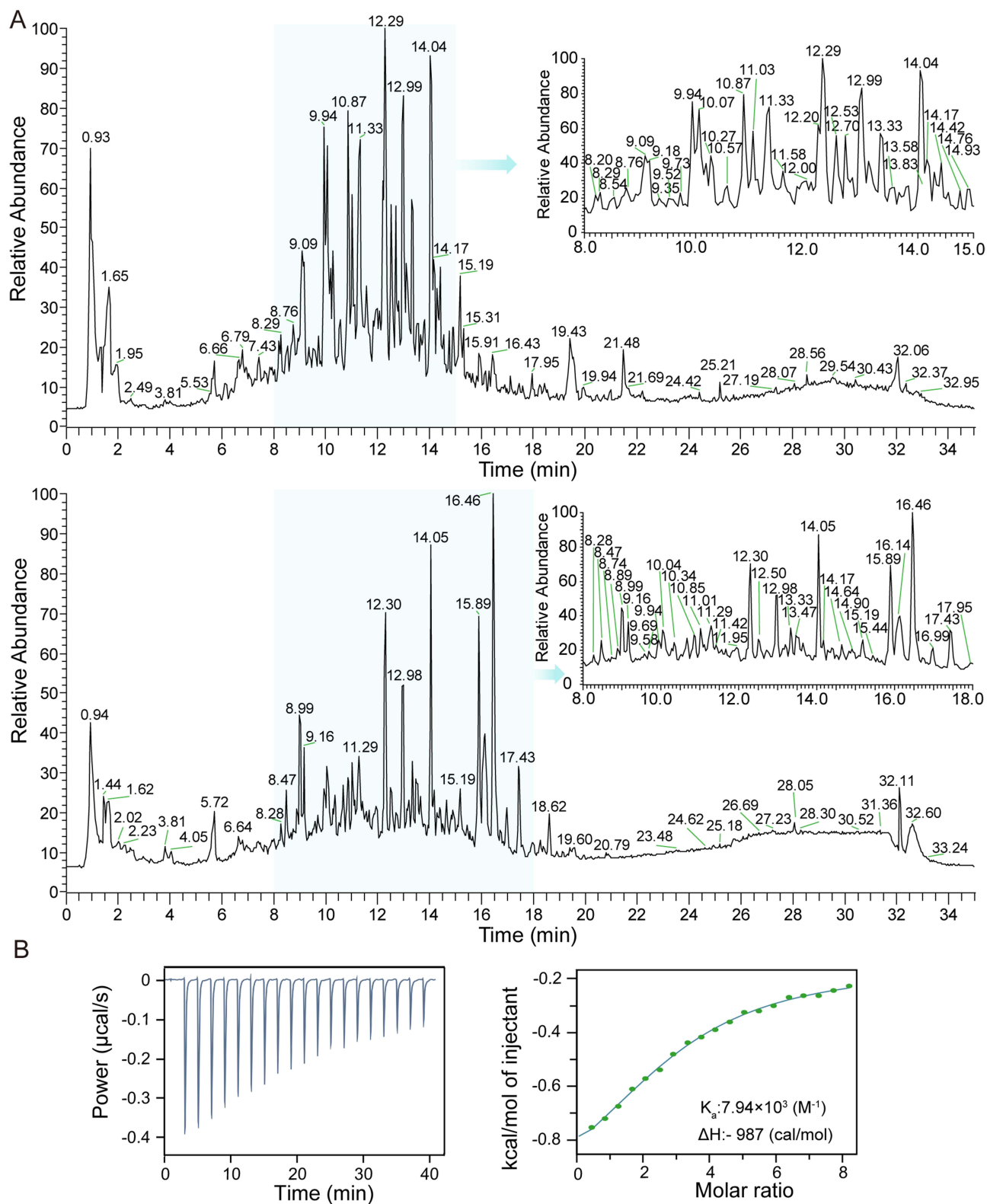
**Figure 3** Identification of the chemical constituents in the herb pair/group (HG) and the binding study between platycodin D (a component of HG) and DSPE-PEG2000 (substance on the surface of LPNs). (**A**) Total ion chromatograms of HG through ultra-high-performance liquid chromatography combined with an Orbitrap mass spectrometer (UHPLC-LTQ-Orbitrap-MS/MS). Upper panel, negative ion mode of HG; lower panel, positive ion mode of HG. (**B**) Isothermal titration calorimetry assay via calorimetric titration of platycodin D (0.075 mM) with DSPE-PEG2000 (3 mM; 25 °C). Left panel, raw data; Right panel, binding isotherm graphs (points, binding isotherm; solid line, fitting curve according to the one-site model).

in SERS, which provided a basis for illustrating the SERS findings and further revealing the interaction between HG and nanoparticles.

Subsequently, the direct binding between platycodin D (a component from the HG) and DSPE-PEG2000 (a substance present on the surface of LPN) was assessed using ITC. An ITC thermogram (Figure 3B) showed the enthalpy changes when platycodin D was injected into the DSPE-PEG2000 solution. The reaction was exothermic with a molar enthalpy change of $\Delta H = -987$ calories/mol and a binding constant ($K_a$) of $7.94 \times 10^3$ ($M^{-1}$). The results indicated that platycodin D is capable of binding to DSPE-PEG2000.

## HNS is Stable in the Lumen and Increases Mucus Transfer

The stability of the HNS in the lumen was evaluated in simulated gastric fluid (SGF) and simulated intestinal fluid (SIF). The results pertaining to the particle size (Figure 4A) and zeta potential (Figure 4B) of the HNS were stable in SGF and SIF from 2 to 4 h, which allowed for the subsequent mucus diffusion and intestinal absorption. An approximately 2-fold increase in particle size for the HNS in SGF may be related to the slight aggregation of individual particles under acidic conditions during the first 2 h. This is also consistent with the change in zeta potential. A decrease in the absolute value of zeta potential occurred at the same time, possibly due to the adsorption of the oppositely charged ion in SGF, which indicates the driving force of particle aggregation.
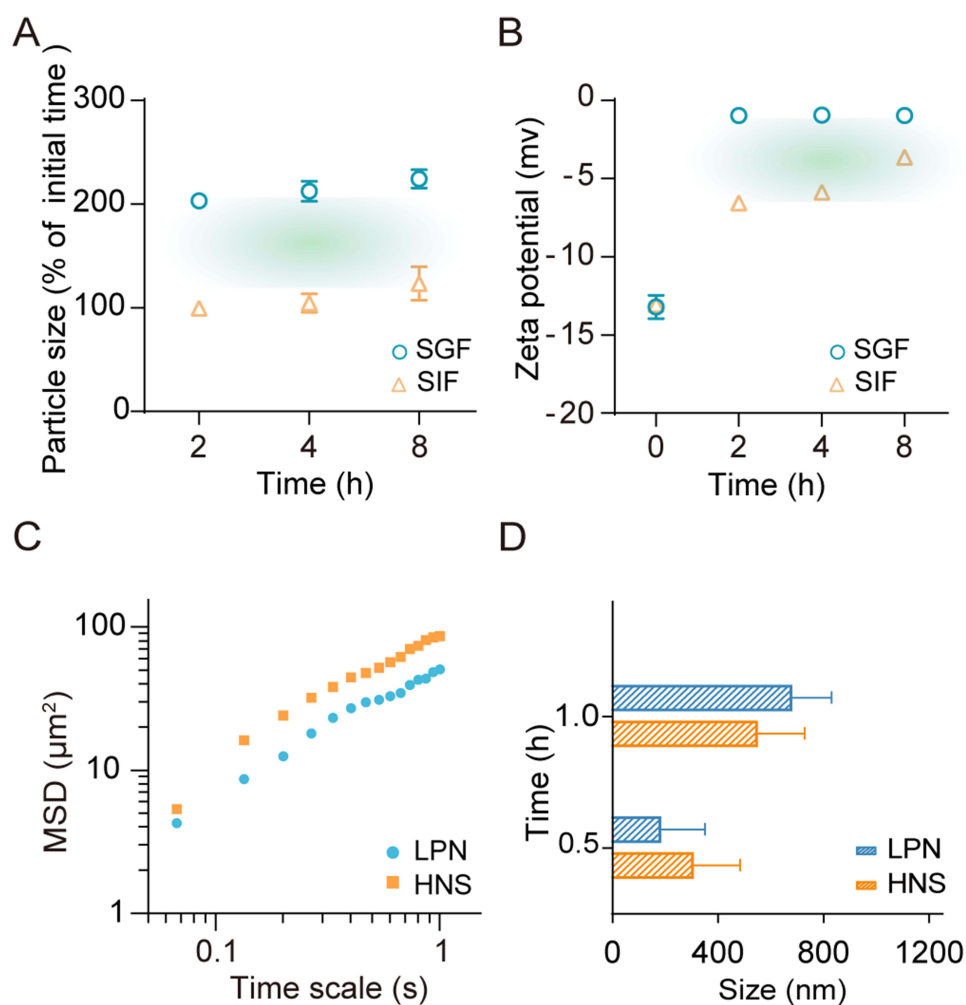


**Figure 4** Physical stability of the HNS in gastrointestinal fluid and evaluation of overcoming the mucus barrier. (**A**) Particle size and (**B**) zeta potential of the HNS in simulated gastric fluid (SGF) and simulated intestinal fluid (SIF) at 37 °C. (**C**) Mean square displacement (MSD)–time curve analysis of CdSe/ZnS quantum dot-labeled nanoparticles. (**D**) Peak frequency distribution of coumarin-6-labeled nanoparticles in mucus determined via nanosight analysis. (mean ± SD, n = 3).

The mean square displacement (MSD)–time curve analysis of nanoparticle mobility in the mucus is shown in Figure 4C. The analysis revealed that the MSD of the HNS was higher than that of LPNs over the same period, indicating that HG association might promote nanoparticle movement in the mucus. As shown in Figure 4D, when the nanoparticles were incubated with the mucus, the particle size increased with time, suggesting that the nanoparticles interacted with endogenous mucus components and attached to or covered the nanoparticle surface, thereby increasing particle size. Notably, the decrease in the peak frequency distribution (the particle size most observed) of the HNS incubated with the mucus for 1 h in comparison to LPNs might be related to the decreased attachment or association of endogenous mucus components, which might denote a moderate regulation of mucus–nanoparticle interactions. Therefore, the HG association might reduce the interactions between the nanoparticle and endogenous mucus components.

For oral nanocarriers, various strategies to improve their mucus penetration capacity have focused on altering the hydrophilicity of the nanoparticle surface, shape, charge, and rigidity.[34,35] Improvement of nanoparticle mucus penetration via multiple strategies could be more efficient than any single strategy devised to liberate the nanoparticles during mucus transfer. Increasing surface hydrophilicity may improve the mucus penetration capacity of nanoparticles.[36] In this study, as revealed in SERS and UPLC-MS, HG dispersions contain certain hydrophilic components, such as phenolic acid, glycosides, and amphiphilic saponins, as surfactants, which may improve the surface hydrophilicity of nanoparticles and facilitate their mucus penetration.

## HNS Increases Uptake by the Villi and Absorption by Peyer's Patches in Mice

We then evaluated the intestinal distribution of the HNS in vivo. Nanoparticles were administered directly to the mouse jejunum, and the cross-sectional nanoparticle distribution in the jejunum was evaluated using a CLSM (Figure 5A). The nanoparticles were loaded with coumarin-6 to track the transfer and diffusion through the mucus and the cells and the lipophilic cell membrane stain DiI to indicate cellular interactions. According to Figure 5A, the signal obtained from the HNS was clearly visible inside the villi and had a higher intensity than that from the LPN group, indicating that HG association promoted the uptake of nanoparticles by villi. Considering this result, we subsequently determined whether the HG association improved the nanoparticle intestinal absorption by affecting the tight junctions between intestinal cells. We used FITC-dextran (FD-4), a 4 kDa fluorescent marker, to track the transport through a cell monolayer and test if HG regulated the tightness of intercellular connections. Compared with that in the FD-4 group, FD-4 accumulation in
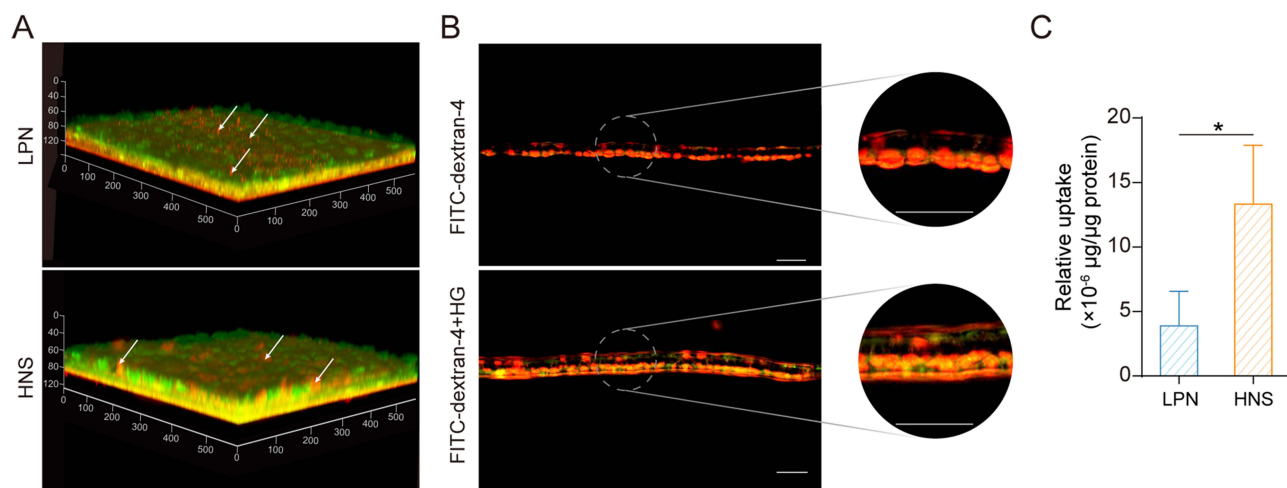


**Figure 5** Uptake of nanoparticles by villi and absorption by Peyer's patches in vivo. (**A**) Nanoparticle diffusion and uptake by villi in the mouse jejunum in vivo. Mice were administered LPNs (top) and the HNS (bottom), in which equal volumes of nanoparticles labeled with coumarin-6 (green signal) and nanoparticles labeled with DiI (red signal) were applied to the jejunum sections for 20 min. The CLSM images show three-dimensional reconstruction (3D) obtained via scanning from the top of the lumen surface to the bottom. The arrows show the distribution of the internalized nanoparticles. Scale bars, 50 μm. (**B**) Side-view confocal micrograph images of FITC-dextran (FD-4) distribution in the presence of HG (0.25 mg/mL) in the Caco-2/HT29-MTX-E12 cell monolayers in vitro (green, FD-4; red, cell nuclei stained with propidium iodide). Scale bar, 50 μm. (**C**) Absorption of nanoparticles by Peyer's patches in mice. (n = 3) (means ± SD, *P < 0.05).

the Caco-2/HT29-MTX-E12 cell monolayer was elevated in the presence of HG (Figure 5B), indicating that HG regulated tight junctions between cells. In vivo Peyer's patches absorption of nanoparticles was measured in mice. As shown in Figure 5C, HNS increased absorption via Peyer's patches in vivo ($p<0.05$). On the one hand, HG regulated the tight junction between cells (Figure 5B), which offered an alternative cell pathway for transport. On the other hand, absorption of nanoparticles by Peyer's patches was influenced by the particle size, hydrophobicity, and surface characteristics of the nanoparticles.[37] The changes in the surface of nanoparticles due to the association of HG might contribute to the enhanced absorption by Peyer's patches. Several polysaccharides from herbal medicines have been reported to be incorporated by M-cells. Alternative pathways, such as paracellular and transcellular pathways, might also favor the absorption through Peyer's patches.

## Translocation into the Systemic Circulation and Biodistribution in Tumors and Lungs

The HNS showed improved mucus penetration and cellular endocytosis in vitro. The in vivo pharmacokinetics of the HNS and LPNs labeled with aggregation-causing quenching probe P2 were investigated. Because it possesses an aza-BODIPY parental structure, P2 is an environment-responsive fluorescence probe that emits fluorescence when loaded onto nanoparticles and shows immediate and absolute fluorescence quenching upon being released into the aqueous phase caused by the disintegration of the nanoparticles.[26] The profile of the fluorescence intensity of nanoparticles in blood vs time is shown in Figure 6A, which demonstrates the absorption of nanoparticles in their integral form. The maximum accumulated signals appeared at 8 h post-oral administration. In addition, the HNS showed higher fluorescence signal intensities than LPNs at the detected time point, which was consistent with the in vitro mucus penetration and
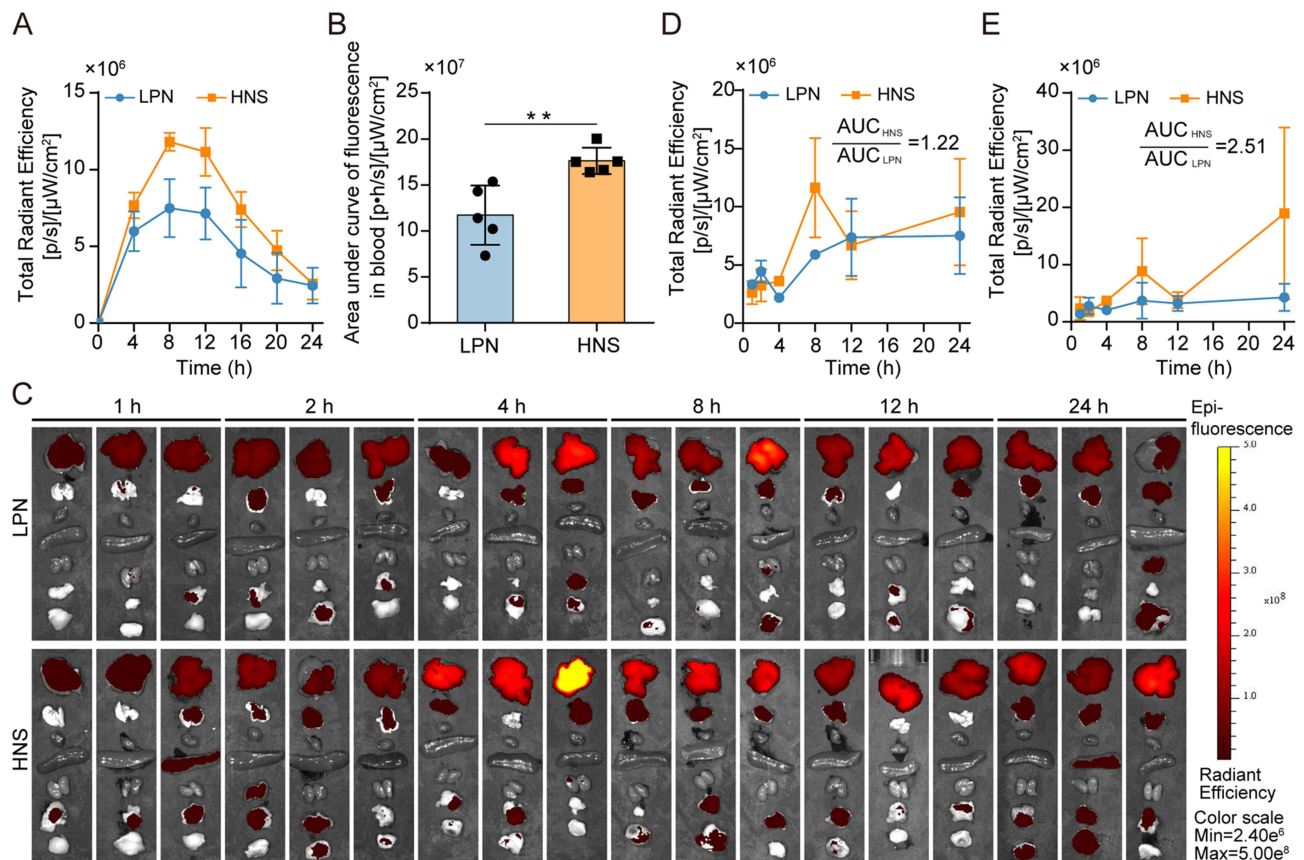


**Figure 6** Translocation of nanoparticles into the systemic circulation and their biodistribution. (**A**) Total radiant efficiency of fluorescence signals in the blood following oral administration of P2-labeled LPNs or the HNS in rats (n = 5). (**B**) Area under the curve of fluorescence signal intensity in the blood vs time following oral administration of P2-labeled LPNs or the HNS in rats (n = 5). (**C**) Ex vivo imaging of liver, lung, heart, spleen, kidney, mesentery, and tumor tissues (from top to bottom) of 4T1 tumor-bearing mice treated with LPNs or the HNS via oral administration. Fluorescence signal quantification of P2 intensity in the lung (**D**) and tumor tissues (**E**) of 4T1 tumor-bearing mice treated with LPNs or the HNS via oral administration (n = 5). (means ± SD, **$P< 0.01$).

nanoparticle absorption in villi in mice. The HNS also showed a significantly higher area under the curve (AUC) ($p<0.01$) (Figure 6B), which suggested that both LPNs and the HNS may overcome the intestinal physiological barriers and enter the circulatory system. More importantly, the improved translocation of nanoparticles into the systemic circulation was found in the group HNS, which enabled increased nanoparticle distribution in the tissues, exerting enhanced therapeutic action. The real-time biodistribution of nanoparticles in 4T1 tumor-bearing mice is shown in Figure 6C. The increased distribution at the target site was beneficial for improved therapeutic effects. The AUC of nanoparticle distribution in the lung (Figure 6D) and tumor tissues (Figure 6E) for the HNS was 1.22-fold and 2.51-fold that of those treated with LPNs, respectively, indicating that the HNS showed enhanced biodistribution in the lung and tumor tissues. The altered biodistribution in the HNS compared with LPNs may have been due to the improved behavior in overcoming intestinal mucus and epithelial barriers. In addition, the enhanced absorption at Peyer's patches in HNS provided possible transport via lymphatic circulation, enabling increased exposure to lymphatic organs. In a previous study,[37] nanoparticles with increased distribution in Peyer's patches following oral administration were shown to promote their targeting to the lung tissue, which suggests that targeted lung delivery may be facilitated through the uptake by Peyer's patches. This was followed by channelization into lymphatic organs, which favors the biodistribution of nanoparticles to lymphatic organs, such as the lung. Whether HG may alter the silibinin pharmacokinetic and biodistribution in tissues needs to be further investigated in the future.

## HNS Alleviates Breast Cancer Metastasis in vivo

We evaluated the alleviation of breast cancer metastasis from HG, silibinin-loaded LPNs, and silibinin-loaded HNS in 4T1 tumor-bearing mice. The HNS significantly reduced the number of metastatic nodules in mouse lung tissue compared with that in the saline group ($p < 0.0001$) (Figure 7A), indicating its ability to alleviate lung metastasis.
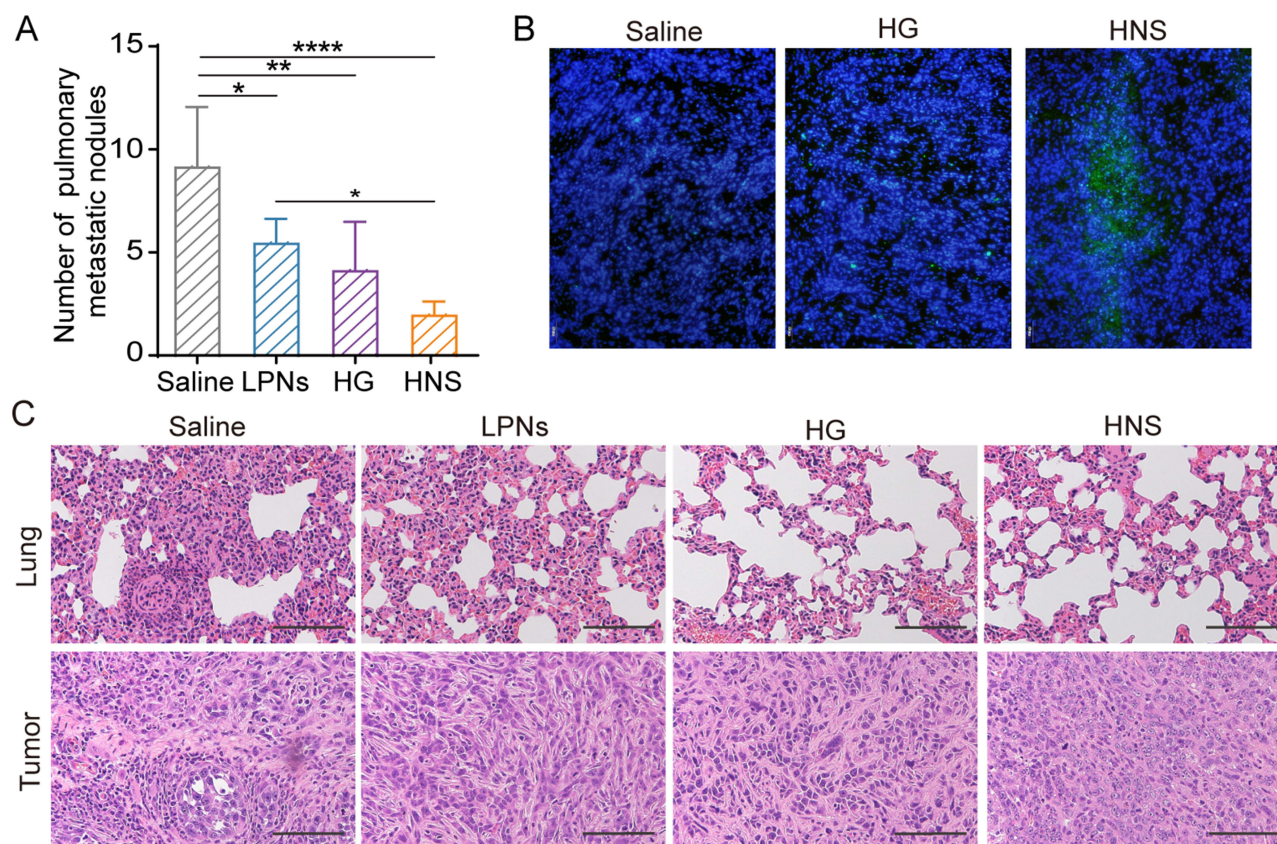


Figure 7 Alleviation of metastasis in 4T1 tumor-bearing mice. (**A**) Lung nodules in tumor-bearing mice under the indicated treatments (mean ± SD, n = 5). (**B**) Effects of different treatments on the apoptosis of tumor tissue. (**C**) Hematoxylin and eosin (H&E) staining of tumor and lung tissues from 4T1 tumor-bearing mice subjected to different treatments. Scale bar, 100 μm. (mean ± SD, *$P < 0.05$; **$P < 0.01$; ****$P< 0.0001$).

Moreover, a visible green fluorescence signal was observed during TUNEL staining in the group treated with the HNS (Figure 7B), which indicated that the HNS-induced apoptosis in the tumor cells. The results of hematoxylin and eosin (H&E) staining are shown in Figures 7C and S8. Some tumor thrombi were apparent in the control group but not in the HNS group. Furthermore, as shown in Figure S8A, some extramedullary hematopoietic foci were apparent in the liver tissue of the saline-treated group.

To understand the molecular mechanism underlying the metastasis alleviation effect of the HNS, we performed immunohistochemical (IHC) assays. MMP-9 and TGF-β1 are involved in metastatic progression, in which the former remodels the extracellular matrix (ECM) and induces angiogenesis, while the latter induces epithelial to mesenchymal transition (EMT).[38,] As shown in Figures 8A and S8B, the expression levels of MMP-9 were reduced in tumor tissues, and those of MMP-9 were reduced in the lung tissues of the HNS group compared with those of the control group. The HNS reduced the expression levels of MMP-9 in the tumor and lung tissues and that of TGF-β1 in the tumors, revealing that the HNS inhibited metastasis by inhibiting tumor angiogenesis and ECM decomposition and alleviating EMT.

Both silibinin and the components in the HG, such as chlorogenic acid, platycodin D, and α-linolenic acid, have shown immune microenvironment modulation effects.[39–41] Therefore, we evaluated whether the HNS would facilitate T-cell infiltration in tumor tissues. Immunosuppressive myeloid-derived suppressor cells (MDSCs) in tumor tissues were analyzed using immunofluorescence staining (Figure 8B). The population of Gr-1$^+$ CD11b$^+$ MDSC cells in the tumor tissue treated by HNS was reduced. Flow cytometry was used to analyze the immunoregulatory cell populations. HNS
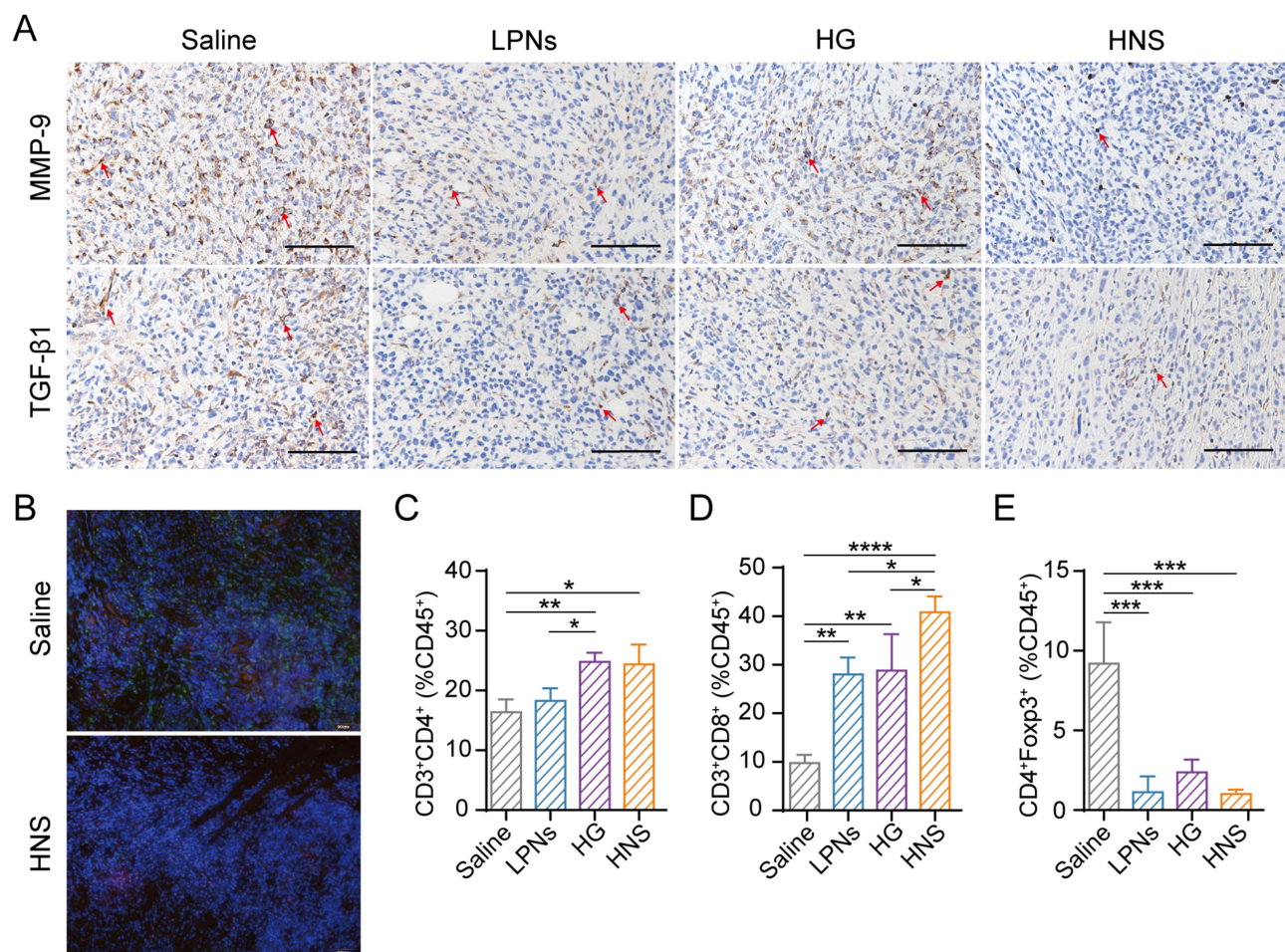


**Figure 8** Immunomodulatory effects of the HNS. (**A**) Immunohistochemical staining of MMP-9 and TGF-β1 in tumor tissues of mice treated with the control, LPNs, HG, or HNS. Scale bar, 100 μm. (**B**) Immunofluorescence staining of MDSCs in tumor-bearing mice treated with saline and the HNS. Scale bar, 100 μm. (**C**) The effect of LPNs, HG, and the HNS on the tumor immune microenvironment of CD4$^+$ CD3$^+$ T cells. (**D**) CD8$^+$ CD3$^+$ T cells and (**E**) regulatory T cells (mean ± SD, n = 3, *P < 0.05; **P < 0.01; ***P < 0.001; ****P< 0.0001).

increased the population of CD8^{+} T cells (Figure 8C and D) and reduced that of Tregs (Figure 8E). Overall, the analysis revealed that HNS may enhance T-cell infiltration in 4T1 tumor-bearing mice and modulate the immune microenvironment.

The formulation of the HG was based on long-term clinical experience. Instead of focusing on a single target, the use of this HG emphasizes the holistic and systemic nature of diseases by targeting multiple sites in vivo. Platycodonis radix contains various active ingredients, including saponins, flavonoids, and phenolic acids, and acts via multiple signaling pathways to inhibit tumor metastasis, eg, by inhibiting tumor cell proliferation, migration, and invasion and inducing tumor cell apoptosis.[42,43] It also activates caspase-3- and caspase-9-dependent apoptotic pathways. Furthermore, platycodin D inhibits the proliferation of MDA-MB-231 tumor cells in BALB/c nude mice by downregulating the epidermal growth factor receptor and reducing MMP9 mRNA expression levels and activity.[43] Germacrone, a component of HG from *Curcuma zedoaria*, may also trigger breast cancer tumor cell apoptosis.[44] Silibinin is a potent F-box protein Skp2-targeting agent.[45,] The induction of apoptosis and suppression of metastasis in HNS in 4T1 tumor bearing mice may be attributed to these factors. The TME acts as the "soil" to support the proliferation of tumor cells and contains blood and lymphatic vessels, extracellular matrix (ECM), carcinoma-associated fibroblasts (CAFs), immune cells, and cytokines. Silibinin regulates the TME by modulating EMT, inhibiting angiogenesis, and decreasing tumor-associated fibroblast and CAF populations. Furthermore, silibinin-loaded nanoparticles abrogate tumor immunosuppression and enhance the anti-tumor immune response by regulating Tregs and MDSCs in the tumor.[21] Certain components of the HG, such as chlorogenic acid, platycodin D, and α-linolenic acid, can regulate T-cell infiltration.[41,42,] Regarding the treatment of metastatic breast cancer, the HG has been used to guide drugs to the lung tissue and reduce metastasis. In the current study, oral intestinal absorption and the biodistribution at the site of action were improved in the HNS. Platycodonis radix is regarded as a meridian-guiding Chinese material medica with in vivo biopharmaceutical activity and therapeutic effects.[46,47] Collectively, multiple mechanisms, including improving biological processes, inducing tumor cell apoptosis, and regulating the TME, may contribute to the alleviation of breast cancer metastasis by the HNS. However, tumor metastasis is a complex process, and whether the HNS inhibits metastasis through alternative pathways or mechanisms, such as mitochondrial impairment or tumor-associated macrophage polarization, should be further investigated. More details in the exocytosis process of HNS and the underlying mechanism, as well as the in vivo structural stability, have yet to be fully elucidated in future research.

## Conclusions

In this study, we report a versatile nanoparticle hybrid delivery system with surface self-binding of components from natural herb pairs, which aid in both oral drug delivery and therapeutic effects. The surface components of the HNS are mainly composed of phenol acids, saponins, and glycosides from the HG. Owing to its unique surface chemistry, the HNS improved the translocation of nanoparticles into systemic circulation by enhancing mucus penetration, intestinal absorption, and Peyer's patch absorption in vivo. Furthermore, the HNS showed improved distribution in tumor tissue and metastatic foci of lung tissue in 4T1 tumor-bearing mice. Oral administration of the HNS alleviated breast cancer metastasis in 4T1 tumor-bearing mice, which was attributed to the induction of tumor apoptosis and altering the structure and immunologic balance of TME. Therefore, the current functional HNS overcame intestinal biological barriers and potentiated therapeutic effects on both tumor cells and the TME, providing fresh insight into the rational development of the nanoparticle-herb hybrid system for alleviating breast cancer metastasis via a convenient route in the near future. Future investigations are warranted to elucidate this process and the underlying mechanisms in vivo.

## Data Sharing Statement

All data are included in this manuscript.

## Ethics Approval and Consent to Participate

All animal procedures were approved by the Institutional Animal Care and Use Committee of the Shanghai University of Traditional Chinese Medicine (Shanghai, China).

## Consent for Publication

All the authors agree to publication.

## Disclosure

The authors declare that there are no competing interests in this work.

## References

1. Ganesh K, Massagué J. Targeting metastatic cancer. *Nat Med*. 2021;27(1):34–44. doi:10.1038/s41591-020-01195-4
2. Klein CA. Cancer progression and the invisible phase of metastatic colonization. *Nat Rev Cancer*. 2020;20(11):681–694. doi:10.1038/s41568-020-00300-6
3. Rao L, Wu L, Liu ZD, et al. Hybrid cellular membrane nanovesicles amplify macrophage immune responses against cancer recurrence and metastasis. *Nat Commun*. 2020;11(1):4909. doi:10.1038/s41467-020-18626-y
4. Bahmani B, Gong H, Luk BT, et al. Intratumoral immunotherapy using platelet-cloaked nanoparticles enhances antitumor immunity in solid tumors. *Nat Commun*. 2021;12(1):1999. doi:10.1038/s41467-021-22311-z
5. Landgraf M, Lahr CA, Kaur I, et al. Targeted camptothecin delivery via silicon nanoparticles reduces breast cancer metastasis. *Biomaterials*. 2020;240:119791. doi:10.1016/j.biomaterials.2020.119791
6. Luo C, Sun J, Du YQ, He ZG. Emerging integrated nanohybrid drug delivery systems to facilitate the intravenous-to-oral switch in cancer chemotherapy. *J Control Release*. 2014;176:94–103. doi:10.1016/j.jconrel.2013.12.030
7. Qin JJ, Wang W, Sarkar S, Zhang RW. Oral delivery of anti-MDM2 inhibitor SP141-loaded FcRn-targeted nanoparticles to treat breast cancer and metastasis. *J Control Release*. 2016;237:101–114. doi:10.1016/j.jconrel.2016.07.008
8. Liu Y, Shen JY, Shi JP, et al. Functional polymeric core-shell hybrid nanoparticles overcome intestinal barriers and inhibit breast cancer metastasis. *Chem Eng J*. 2022;427:131742. doi:10.1016/j.cej.2021.131742
9. Liu Y, Xie XM, Hou XF, et al. Functional oral nanoparticles for delivering silibinin and cryptotanshinone against breast cancer lung metastasis. *J Nanobiotechnology*. 2020;18(1):83. doi:10.1186/s12951-020-00638-x
10. Qiao L, Yang HS, Gao SJ, Li L, Fu XJ, Wei QC. Research progress on self-assembled nanodrug delivery systems. *J Mater Chem B*. 2022;10 (12):1908–1922. doi:10.1039/D1TB02470A
11. Wu JN, Han XH, Ye YY, Huang M, Liu S. Effect of platycodon with different treatments of traditional Chinese medicine on Smad4, Samd7 and TGFβ1 in breast cancer pulmonary metastasis mice. *Chin J Traditional Med Sci Tech*. 2013;20:247–249. Chinese.
12. Zhang Z, Zhao M, Zheng W, Liu Y. Platycodin D, a triterpenoid saponin from Platycodon grandiflorum, suppresses the growth and invasion of human oral squamous cell carcinoma cells via the NF-κB pathway. *J Biochem Mol Toxicol*. 2017;31(9):e21934. doi:10.1002/jbt.21934
13. Lin YC, Lin CH, Yao HT, et al. Platycodon grandiflorum (PG) reverses angiotensin II-induced apoptosis by repressing IGF-IIR expression. *J Ethnopharmacol*. 2017;205:41–50. doi:10.1016/j.jep.2017.04.028
14. Ye YY, Pei LX, Wu CY, Liu S. Protective effect of traditional Chinese medicine formula RP on lung microenvironment in pre-metastasis stage of breast cancer. *Integr Cancer Ther*. 2019;18:1534735419876341. doi:10.1177/1534735419876341
15. Choi JH, Hwang YP, Kim HG, et al. Saponins from the roots of Platycodon grandiflorum suppresses TGFβ1-induced epithelial-mesenchymal transition via repression of PI3K/Akt, ERK1/2 and Smad2/3 pathway in human lung carcinoma A549 cells. *Nutr Cancer*. 2014;66(1):140–151. doi:10.1080/01635581.2014.853087
16. Qi HY, Ning L, Yu ZY, Dou GJ, Li L. Proteomic identification of eEF1A1 as a molecular target of curcumol for suppressing metastasis of MDA-MB-231 cells. *J Agric Food Chem*. 2017;65(14):3074–3082. doi:10.1021/acs.jafc.7b00573
17. Li Y, Xia Q, Zhao RZ, Deng SG. Effects of platycodon grandiflorum on the distribution of cisplatin in orthotopic lung cancer transplantation of nude mice. *Pharmacology and Clinics of Chinese Materia Medica*. 2018;34(2):71–75.Chinese:
18. Xu YW, Geng SN, Wang YH, Du GJ. Guiding mechanism of platycodin D in treatment of mouse lung cancer with doxorubicin. *Zhongguo Zhong Yao Za Zhi*. 2021;46(6):1480–1489. Chinese. doi:10.19540/j.cnki.cjcmm.20201027.402
19. Li Y, Guo CJ, Chen Q, et al. Improvement of pneumonia by curcumin-loaded bionanosystems based on platycodon grandiflorum polysaccharides via calming cytokine storm. *Int J Biol Macromol*. 2022;202:691–706. doi:10.1016/j.ijbiomac.2022.01.194
20. Jiang M, He KY, Qiu T, et al. Tumor-targeted delivery of silibinin and IPI-549 synergistically inhibit breast cancer by remodeling the microenvironment. *Int J Pharm*. 2020;581:119239. doi:10.1016/j.ijpharm.2020.119239
21. Huo MR, Wang HL, Zhang Y, et al. Co-delivery of silybin and paclitaxel by dextran-based nanoparticles for effective anti-tumor treatment through chemotherapy sensitization and microenvironment modulation. *J Control Release*. 2020;321:198–210. doi:10.1016/j.jconrel.2020.02.017
22. Lin CH, Li CH, Liao PL, et al. Silibinin inhibits VEGF secretion and age-related macular degeneration in a hypoxia-dependent manner through the PI-3 kinase/Akt/mTOR pathway. *Br J Pharmacol*. 2013;168(4):920–931. doi:10.1111/j.1476-5381.2012.02227.x
23. Ma ZW, Tang JW, Liu QH, et al. Identification of geographic origins of Morus alba Linn. through surfaced enhanced Raman spectrometry and machine learning algorithms. *J Biomol Struct Dyn*. 2023;41(23):14285–14298. doi:10.1080/07391102.2023.2180433

24. Liu Y, Liu JG, Liang J, et al. Mucosal transfer of wheat germ agglutinin modified lipid-polymer hybrid nanoparticles for oral delivery of oridonin. *Nanomedicine*. 2017;13(7):2219–2229. doi:10.1016/j.nano.2017.05.003

25. Maisel K, Ensign L, Reddy M, Cone R, Hanes J. Effect of surface chemistry on nanoparticle interaction with gastrointestinal mucus and distribution in the gastrointestinal tract following oral and rectal administration in the mouse. *J Control Release*. 2015;197:48–57. doi:10.1016/j.jconrel.2014.10.026

26. He HS, Wang LT, Ma YH, et al. The biological fate of orally administered mPEG-PDLLA polymeric micelles. *J Control Release*. 2020;327:725–736. doi:10.1016/j.jconrel.2020.09.024

27. Du MH, Sun ZQ, Xie MZ, Gu SQ, Chen YC, Wang Q. A new method for rapid identification of traditional Chinese medicine based on a new silver sol: using the SERS spectrum for quality control of flavonoids and flavonoid glycosides in Potentilla discolor Bge. *J Mater Chem C*. 2023;11 (43):15138–15148. doi:10.1039/D3TC02768F

28. Xu YK, Zhang YR, Li CC, Ye ZW, Bell SEJ. SERS as a probe of surface chemistry enabled by surface-accessible plasmonic nanomaterials. *Acc Chem Res*. 2023;56(15):2072–2083. doi:10.1021/acs.accounts.3c00207

29. Guimarães PCL, da Silva JR, de Azevedo RB, Morais PC, da Silva SW. Fabrication and characterization of glycine-loaded PEG nanoparticles for drug delivering: a comprehensive SERS study. *Appl Surf Sci*. 2018;450:396–403. doi:10.1016/j.apsusc.2018.04.211

30. Kong SN, Ou S, Liu Y, et al. Surface-enhanced raman spectroscopy analysis of astragalus saponins and identification of metabolites after oral administration in rats by ultrahigh-performance liquid chromatography/quadrupole time-of-flight mass spectrometry analysis. *Front Pharmacol*. 2022;13:828449. doi:10.3389/fphar.2022.828449

31. Zhang W, Wang YP, Bai XY, Zhao B. Based on SERS conformational studies of ginsenoside Rb1 and its metabolites before and after combined with human serum albumin. *Spectrochim Acta A Mol Biomol Spectrosc*. 2015;137:116–121. doi:10.1016/j.saa.2014.08.051

32. Xiao MX, Chen YQ, Zheng FL, et al. Predicting the storage time of green tea by myricetin based on surface-enhanced Raman spectroscopy. *NPJ Sci Food*. 2023;7(1):28. doi:10.1038/s41538-023-00206-1

33. Sánchez-Cortés S, García-Ramos JV. Adsorption and chemical modification of phenols on a silver surface. *J Colloid Interface Sci*. 2000;231 (1):98–106. doi:10.1006/jcis.2000.7101

34. Wu JW, Zheng YX, Liu M, Shan W, Zhang ZR, Huang Y. Biomimetic viruslike and charge reversible nanoparticles to sequentially overcome mucus and epithelial barriers for oral insulin delivery. *ACS Appl Mater Interfaces*. 2018;10(12):9916–9928. doi:10.1021/acsami.7b16524

35. Yu MR, Xu L, Tian FL, et al. Rapid transport of deformation-tuned nanoparticles across biological hydrogels and cellular barriers. *Nat Commun*. 2018;9(1):2607. doi:10.1038/s41467-018-05061-3

36. Cui Y, Shan W, Liu M, Wu L, Huang Y. A strategy for developing effective orally-delivered nanoparticles through modulation of the surface "hydrophilicity/hydrophobicity balance". *J Mater Chem B*. 2017;5(6):1302–1314. doi:10.1039/C6TB02475K

37. Bachhav SS, Dighe VD, Devarajan PV. Exploring Peyer's patch uptake as a strategy for targeted lung delivery of polymeric rifampicin nanoparticles. *Mol Pharm*. 2018;15:10 4434–4445. doi:10.1021/acs.molpharmaceut.8b00382

38. Cabral-Pacheco GA, YGarza-Veloz I, Castruita-De la Rosa C et al, et al. The roles of matrix metalloproteinases and their inhibitors in human diseases. *Int J Mol Sci*. 2020;21(24):9739. doi:10.3390/ijms21249739

39. Zhang Y, Yang YF, Ye J et al, et al. Construction of chlorogenic acid-containing liposomes with prolonged antitumor immunity based on T cell regulation. *Sci China Life Sci*. 2021;64(7):1097 1115. doi:10.1007/s11427-020-1739-6

40. Vara-Messler M, Pasqualini ME, Comba A, et al. Increased dietary levels of α-linoleic acid inhibit mammary tumor growth and metastasis. *Eur J Nutr*. 2017;56(2):509–519. doi:10.1007/s00394-015-1096-6

41. Yang RJ, Pei TL, Huang RF, et al. Platycodon grandiflorum triggers antitumor immunity by restricting PD-1 expression of CD8+ T cells in local tumor microenvironment. *Front Pharmacol*. 2022;13:774440. doi:10.3389/fphar.2022.774440

42. Yu JS, Kim AK. Platycodin D induces apoptosis in MCF-7 human breast cancer cells. *J Med Food*. 2010;13(2):298–305. doi:10.1089/jmf.2009.1226

43. Chun J, Kim YS. Platycodin D inhibits migration, invasion, and growth of MDA-MB-231 human breast cancer cells via suppression of EGFR-mediated Akt and MAPK pathways. *Chem Biol Interact*. 2013;205(3):212–221. doi:10.1016/j.cbi.2013.07.002

44. Zhong ZF, Chen XP, Tan W et al. Germacrone inhibits the proliferation of breast cancer cell lines by inducing cell cycle arrest and promoting apoptosis. *Eur J Pharmacol*. 2011;667(1–3):50–55. doi:10.1016/j.ejphar.2011.03.041

45. Zhang SB, Hong M, Sun XY, et al. Silybin has therapeutic efficacy against non-small cell lung cancer through targeting of Skp2. *Acta materia medica*. 2022;1(3):302–313. doi:10.15212/AMM-2022-0011

46. Zhang F, Zhan Q, Gao SH, et al. Chemical profile- and pharmacokinetics-based investigation of the synergistic property of platycodonis radix in traditional Chinese medicine formula Shengxian decoction. *J Ethnopharmacol*. 2014;152(3):497–507. doi:10.1016/j.jep.2014.01.033

47. Hao W, Shi YY, Qin YN, et al. Platycodon grandiflorum protects against anthracycline-induced cardiotoxicity in early breast cancer patients. *Integr Cancer Ther*. 2020;19:1534735420945017. doi:10.1177/1534735420945017